J. Fluid Mech. (1999), *vol.* 378, *pp.* 319–334. Printed in the United Kingdom

Rising speed and dissolution rate of a carbon dioxide bubble in slightly contaminated water

By F. TAKEMURA AND A. YABE

Mechanical Engineering Laboratory, Agency of Industrial Science and Technology (AIST),
Ministry of International Trade and Industry (MITI), 1-2 Namiki, Tsukuba, Ibaraki 305, Japan

(Received 1 May 1998 and in revised form 20 August 1998)

The rising speed and dissolution rate of a carbon dioxide bubble in slightly contaminated water were investigated experimentally and numerically. We developed an experimental system that uses a charged-coupled device (CCD) camera coupled with a microscope to track the rising bubble. By precisely measuring the bubble size and rising speed, we were able to accurately estimate the drag coefficient and the Sherwood number for the dissolution rate of gas bubbles at Reynolds numbers below 100 in the transient regime, where the bubble changes from behaving as a fluid sphere to behaving as a solid particle. We also numerically estimated the drag coefficient and Sherwood number of the 'stagnant cap model' by directly solving the coupled Navier–Stokes and convection–diffusion equations. We compared our experimental results with our numerical results and proposed equations for estimating the drag coefficient and Sherwood number of the bubble affected by contamination and clarified that the gas–liquid interface of the carbon dioxide bubble in water is immobile. We also show that the experimental and numerical results are in good agreement and the stagnant cap model can explain the mechanism of the transient process where the bubble behaviour changes from that of a fluid sphere to that of a solid particle.

1. Introduction

The gas dissolution process of bubbles rising in water is important in liquid-phase reactions that are often seen in chemical and bioengineering applications. The rising speed of a bubble and the rate of gas dissolution are factors that strongly affect the gas dissolution process. Water contamination influences both the rising speed and the dissolution rate, and is therefore an important aspect of the process.

A bubble in water changes behaviour with increasing amounts of water contamination. When rising in extremely clean water, a bubble behaves like a fluid sphere (Duinveld 1995). Conversely, when rising in very contaminated water, a bubble behaves like a solid particle if it is affected by the contamination (Clift, Grace & Weber 1978). Much research has been performed on this transient regime, and is reviewed by Clift *et al.* (1978) and Cuenot, Magnaudet & Spennato (1997). To date, the 'stagnant cap model', shown in figure 1, has been proposed to explain behaviour in the transition regime. In this model, contamination accumulates from the rear of the bubble, increasing the immobile area of the surface. This immobile area eventually covers the entire surface, and the bubble then behaves as a solid particle. Many researchers have used this model to analyse the effect of contamination on the rising speed of a bubble (Sadhal & Johnson 1983; Fdhila & Duineveld 1996). In particular, Cuenot

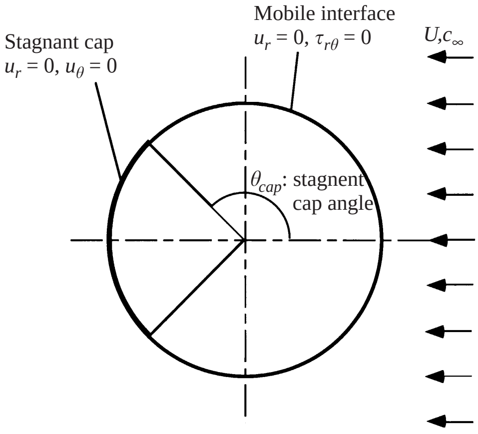

FIGURE 1. Schematic of the stagnant cap model.

et al. (1997) analysed the transient behaviour of drag coefficients in detail, considering the diffusion of contaminants in the water and adsorption and accumulation of contaminants at the bubble surface.

Although the proposed model has been qualitatively confirmed by experiments (Clift *et al.* 1978), few experiments have succeeded in quantitatively confirming it. Fdhila & Duineveld (1996) introduced known organic and ionic materials into the water and measured the concentration and the rising velocity of the bubble. They showed that the drag coefficient increases as the concentration of impure materials increases. To confirm and improve the study of this effect, we made precise measurements of the time histories of the rising speed and compared these with quantitative numerical simulations for the same conditions as the experimental measurements. Because of the difficulty in obtaining complete information about prior experimental conditions and in precisely measuring the time histories of the rising speed, we developed a new method for confirmation of this model.

Many methods have been used to study the gas dissolution process of rising bubbles. Leonard & Houghton (1963) developed an experimental apparatus with a horizontal capillary tube partly filled with mercury at the bottom of a test cell. When the volume of the bubble changed in the liquid, the mercury in the capillary tube moved to keep the liquid pressure constant. They measured the volume change of the bubble from the distance the mercury moved in the capillary tube and estimated the dissolution rates of gas bubbles in water. Calderbank, Johnson & London (1970) measured the dissolution rates of bubbles using a mechanism in which the volume of a bubble in a liquid in a closed system did not change due to dissolution, but the liquid pressure did change. The measurement of the bubble sizes was not precise in these experiments because they measured it indirectly. Using laser-Doppler anemometry, Brankovic, Currie & Martin (1984) developed a system for directly measuring the rising speed and bubble size simultaneously. They continuously released bubbles of almost the same size and measured the bubble size and the rising speed at various positions by moving a test column up and down. They transformed the radius change of the bubble as a function of the position into time histories of the bubble radius, using the profile of the rising speed. From these time histories, they estimated the value of the Sherwood number, *Sh*. Although these experiments directly measured bubble size, deviation in the bubble sizes created large uncertainty in the results.

Detsch & Harris (1989) investigated dissolution rates and rise velocities of small air bubbles in pure water and in salt water. They measured the bubble size directly using a microscope with a video camera and estimated the dissolution rate of the bubble. Their experimental results agree relatively well with theoretical results.

Recently, we developed an experimental apparatus in which a charged-coupled device (CCD) camera with a microscope follows the rising bubble and precisely measures changes in the bubble size and the rising speed when a spherical oxygen gas bubble dissolves in silicon oil. We also estimated Sh as a function of Schmidt and Reynolds numbers based on changes in the bubble size and the rising speed. By directly solving the Navier–Stokes and the convection–diffusion equations, we numerically estimated the Sherwood number for dissolution of a spherical gas bubble in an infinite liquid, and showed that the numerical results agree well with the experimental results for the drag coefficients and Sherwood number (Takemura & Yabe 1998)

The time scale of the dissolution process of a gas bubble into a liquid is much longer than the development time of the velocity and concentration boundary layer (Takemura & Yabe 1998). Thus, values of measured drag coefficients and dissolution rates in experiments can be regarded as the same as those at steady state. In our study, we used both the dissolution rates and the drag coefficients to confirm the stagnant cap model.

In this study we estimate the drag coefficients and Sherwood number ($Sh = 2R\alpha/D$, where R is the bubble radius, α is the mass transfer coefficient and D is the diffusivity of a gas in a liquid) as a function of the Reynolds number ($Re = 2RU/\nu$, where U is the rising speed, and ν is the kinematic viscosity) based on the changes in R and U, for the dissolution of carbon dioxide bubbles in slightly contaminated water. We used the same apparatus as before for measuring oxygen dissolution in silcon. We also numerically estimate drag coefficients and Sherwood numbers of the stagnant cap model by directly solving the coupled Navier–Stokes and convection–diffusion equations. We compare our experimental results with our numerical results and propose equations for estimating the drag coefficients and Sherwood numbers of a bubble affected by water contamination and clarify that the gas–liquid interface of the carbon dioxide bubble in water is immobile. We demonstrate that the experimental and numerical results agree well in the transition regime where the bubble changes from behaving as a fluid sphere to behaving as a solid particle. We also explain the mechanism of this transition process.

2. Experimental apparatus and procedures

Figure 2 shows a diagram of the apparatus we used to measure the changes in R and U. It consists of a test section, a bubble generator, a storage tank for degassing air, a pressure transducer (Kulite, XTM-190), a vacuum pump, an agitator, a liquid pump, an optical microscope, a CCD camera, a video cassette recorder, a Z-axis stage, a stage controller, a video capture board, and a personal computer (PC) for controlling the system. The test section was a square pipe 40 mm on each side and 500 mm long. The bubble generator consisted of a 0.1 mm thick stainless plate with a 40 μm diameter hole, a solenoid coil, a rod with a rubber stopper, and a spring to keep the hole closed under normal conditions. When an electric current is supplied to the coil, the rod goes down, and when the current is stopped it rises. The bubble generator produced single bubbles of carbon dioxide because the pressure inside the bubble generator at the bottom of the test section was held about 0.5 kPa higher than the

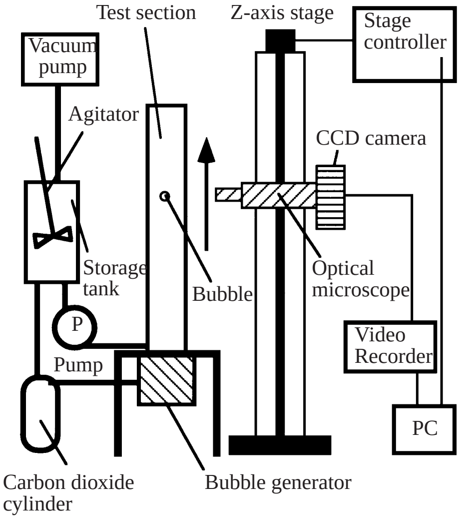

FIGURE 2. Schematic of the experimental apparatus used to monitor and measure changes in a rising bubble.

liquid pressure at the bottom of the test section. The initial size of the bubbles varied from 0.1 to 0.5 mm in radius. The storage tank was used to set the concentration of carbon dioxide in the water that was introduced into the test section. The pressure transducer measured the equilibrium pressure corresponding to the concentration of carbon dioxide in the water.

We did two different experiments. In Case 1 we measured the dissolution rate of bubbles fully affected by contamination, and in Case 2 we measured U and the dissolution rate in the transition of the bubble behaviour from a fluid sphere to a solid particle. The CCD camera that we used had a resolution of 640 × 480 pixels. In Case 1, we calibrated the CCD camera to about 2.5 μm per pixel and took photographs at 30 frames per second. The camera with a optical microscope was connected to the Z-axis stage. To track the rising bubble we controlled the speed of the camera as follows. A picture of the bubble was recorded by the PC via the video capture board at 30 frames per second. A binary image was made and the position of the bubble was calculated. For consecutive frames, we calculated the relative speed between the bubble and the camera and used this relative speed to adjust the speed of the stage.

In Case 2, for the transition experiments we calibrated the CCD camera to about 1.8 μm per pixel and took photographs at 120 frames per second. We used a faster rate because the transition process finishes within 1 s after the bubble is generated. For the same reason, we could not adjust the camera speed to the change in U. Therefore, we took photographs of the bubbles while moving the camera at a constant speed. In both cases, the depth of the field of view of the microscope was around ± 70 μm and the light was supplied from behind.

We used water that was filtered with a water purification system (ADVANTEC, GSH-200). In this apparatus, water passes through activated carbon and an ion exchange resin for eliminating organic materials and metal ions. The water was distilled in a boiler made of hyperhard glass and then refined through an ion exchange resin and membrane filter for high purity. The quality of the water introduced into the storage tank was as follows: the specific resistance was 6.7 MΩ cm and the total concentration of ion materials was less than 0.05 p.p.m. This impurity level is a little worse than that of the water that Duineveld (1995) used. We also measured the number of particles in the size range from 1 to 45 μm using an automatic particle size analysis system (HIAC, PA-720). The water introduced into the test section after degassing in the storage tank included around 300 particles/ml and no particle greater than 15 μm was counted. The quality of the water became worse than the initial condition of several particles per ml, due to exposure to the atmosphere. However, we still regarded the water as only slightly contaminated because the number of particles was smaller than for tap water, which includes around 3000 particles/ml. In addition, because we did not add anything else like organic materials, we can regard the water as mainly contaminated by particles floating in air or adsorbed on the wall of the storage tank and the test section.

We did experiments under atmospheric pressure (101.0 kPa) and room temperature (22.5–23.5 °C). Under these conditions, the kinematic viscosity of water is 0.93 $\mathrm{mm^2\,s^{-1}}$ (Sengers & Watson 1986), the diffusivity and solubility of carbon dioxide in water (Henry's constant based on density) are $1.85 \times 10^{-3}\,\mathrm{mm^2\,s^{-1}}$ (Himmelblau 1956) and 63 MPa (Wilhelm, Battino & Wilcock 1977), respectively, and the Schmidt number $(Sc = \nu/D) \sim 500$.

We used the following experimental procedure. We first removed dissolved air by degassing the water introduced into the storage tank. In the high contamination experiment, we then dissolved pure carbon dioxide into the water to an equilibrium pressure of 70 kPa. Because the solubility of carbon dioxide in water is very high, it is difficult to follow the rising bubble if there is no carbon dioxide dissolved in the water that is introduced into the test section (c_∞). Therefore we dissolved carbon dioxide into water in a closed storage tank until equilibrium between the gas pressure and the gas concentration in the water was achieved. We used a pressure transducer to monitor the gas pressure. In the experiments on the transient regime, we used the degassed water. We introduced the water into the test section and measured both R and U using the recorded pictures and the time history of the camera speed. We measured R in every frame. We calculated U by measuring the position of the centre of the bubble in every frame, calculating the relative speed from the movement of the centre in two consecutive frames, and adding the camera speed corresponding to those two frames.

Figure 3 shows typical photographs taken with the CCD camera. Case 1 is for dissolution of a rising bubble affected by contamination, and Case 2 is for a bubble in the transient regime. In Case 1, the initial R was 0.38 mm, the initial U was 88 $\mathrm{mm\,s^{-1}}$, and the resulting Reynolds number was 72. In Case 2, the initial R was 0.32 mm, the initial U was 135 $\mathrm{mm\,s^{-1}}$, and the resulting Reynolds number was 93, the highest for all of the results. The pictures demonstrate that the bubble rose vertically, because within the 70 μm field of view every photograph is in focus. Therefore, the flow around the bubble retained axial symmetry under our experimental conditions.

We also estimated the non-sphericity of the bubbles from $1 - R_{min}/R_{max}$, where R_{min} and R_{max} are the measured maximum and minimum radius of the bubble, respectively. When R was 0.32 mm, the non-sphericity attains a maximum value of 0.02 and can be regarded as negligibly small. Therefore we were able to assume that the bubbles were spherical under our experimental conditions. It is also well known that deformation of a bubble strongly depends on the Weber number ($We = 2\rho_l U^2 R/\sigma$, where ρ_l is the liquid density and σ is the surface tension) and the bubble deformation is negligibly small when the Weber number is smaller than 0.5 (Ryskin & Leal 1984; Christov & Volkov 1985). In our experiments, the calculated maximum Weber number is approximately 0.17, where the density of the liquid is 997 $\mathrm{kg\,m^{-3}}$ and the surface

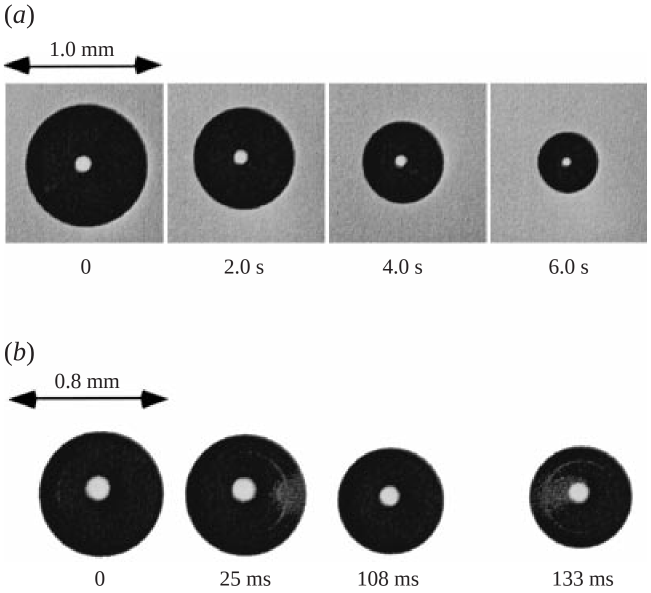

Figure 3. Photographs showing a bubble rising in water. (*a*) Bubble affected by contamination, (*b*) bubble in transition region.

tension is about 70 mN m^{-1} (Uchida *et al.* 1982). Therefore, we can regard the bubbles in our experiments as essentially spherical.

3. Estimation of drag coefficient and Sherwood number

The drag coefficient of a bubble can be calculated from the steady-state balance between the buoyancy and the drag forces. In this experiment, R continuously decreased with time due to dissolution of the gas into the liquid, also causing U to continuously decrease.

We consider the time scale for a bubble to reach steady state in a velocity field, and the resulting concentration field of dissolved gas after the bubble is generated. Mei, Klausner & Lawrence (1994) analysed the effects of the history force on the drag force when the flow around a bubble was changed stepwise. They showed that the effect remains for a long time as Re decreases. Takagi & Matsumoto (1996) numerically analysed the motion of bubble released in a quiescent liquid without an initial velocity component, and showed that the time, t_1, for the drag coefficient to come within 5 % of the drag coefficient at steady state is equal to around $R^2/5\nu$ for $Re = 50$. Clift *et al.* (1978) showed that the time, t_2, for Sh to come within 10 % of Sh at steady state is equal to $1.8R/U$, when the concentration field around a bubble is changed in a stepwise manner. For our experimental conditions, in Case 1 the unsteady term can be neglected, because the maximum values of t_1 and t_2 are 0.04 s and 0.01 s, respectively, and the typical duration of our experiments was longer than 10 s. On the other hand, the typical duration of our experiments in Case 2 was comparable with t_1 (= 0.02 s) and t_2 (= 0.005 s). However, the initial frame (= 0 s) in figure 3 does not show the time when the bubble was generated, but rather the time when the camera first captured the bubble. It takes at least 0.08 s for the camera to capture the bubble because the camera starts to move before the bubble is generated. Therefore, we can assume that the velocity and concentration fields reach steady states. The steady drag coefficient can be calculated as follows:

$$C_D = \frac{8Rg}{3U^2}, \tag{3.1}$$

where g is gravitational acceleration. We estimated the drag coefficients using (3.1). The maximum uncertainty of C_D was estimated to be 4 % by error analysis (Benedict *et al.* 1985) of measurements of the R and U.

We represent the mean mass transfer coefficient, α (see Lochiel & Calderbank 1964), of a spherical bubble as follows:

$$(c_s - c_\infty)\alpha = -\frac{D}{4\pi R^2}\int_0^\pi \left(\frac{\partial c}{\partial r}\right)_s 2\pi R^2 \sin\theta \, \mathrm{d}\theta, \tag{3.2}$$

where c denotes the concentration of gas in the liquid, c_s denotes the concentration at the interface, c_∞ denotes the concentration at infinity, and the subscript s denotes the gas–liquid interface. We can derive the following equation for the mass flux and the change of mass inside the bubble:

$$\frac{\mathrm{d}}{\mathrm{d}t}\left(\tfrac{4}{3}\pi R^3 \rho_g\right) = 2\pi R^2 \rho_l D \int_0^\pi \left(\frac{\partial c}{\partial r}\right)_s \sin\theta \, \mathrm{d}\theta. \tag{3.3}$$

Here, we can equate ρ_g with the gas density inside the bubble without accounting for the vapour pressure, because the diffusion between the vapour and the gas inside the bubble is not the limiting resistance for mass transfer inside the bubble. From (3.2) and (3.3) we can derive the following expression for Sh defined as $2\alpha R/D$:

$$Sh = -\frac{2R}{D(c_s - c_\infty)} \frac{\left(3\dot{R}\rho_g + R\dot{\rho_g}\right)}{3\rho_l}. \tag{3.4}$$

Here, the dot operator denotes a time differential. Equation (3.4) can be transformed as follows by using Henry's Law ($c = p/H$, where p is pressure of gas and H is Henry's constant) and the equation of state:

$$Sh = -\frac{2R}{D(p_g - p_\infty)} \frac{\left(3\dot{R}p_g + R\dot{p_g}\right)}{3} \frac{H}{\rho_l \Re T}, \tag{3.5}$$

where $\Re$ represents the gas constant of carbon dioxide, T the temperature of the liquid, p_g the gas pressure inside the bubble without the vapour pressure and p_∞ the pressure at infinity corresponding to the concentration at infinity ($= c_\infty H$). The term $\dot{p_g}$ can be expressed as $\rho_l g U$ and the ratio of $R\dot{p_g}/(3\dot{R}p_g)$ can be estimated from our experimental results. Because the maximum ratio is 0.02, $R\dot{p_g}$ can be regarded as negligibly small. Therefore (3.5) can be written as

$$Sh = -\frac{2R\dot{R}p_g}{D(p_g - p_\infty)} \frac{H}{\rho_l \Re T}. \tag{3.6}$$

As shown in (3.6), to calculate Sh we must estimate the radius, R, the rate of radius change, $\dot{R}$, and the pressure inside the bubble, p_g. Although we can directly measure R, we need to fit a function of time to the time histories of R and calculate its time differential to estimate the rate of radius change. Figure 4 shows the time histories of the radii for a bubble affected by contamination, Case 1, and in the transition regime, Case 2. In Case 1, the changes in the radii are smooth and can be fitted by a linear function, as shown by the line in figure 4(*a*). In Case 2, the time histories of R in the transient regime can be fitted by a second-order polynomial function, as

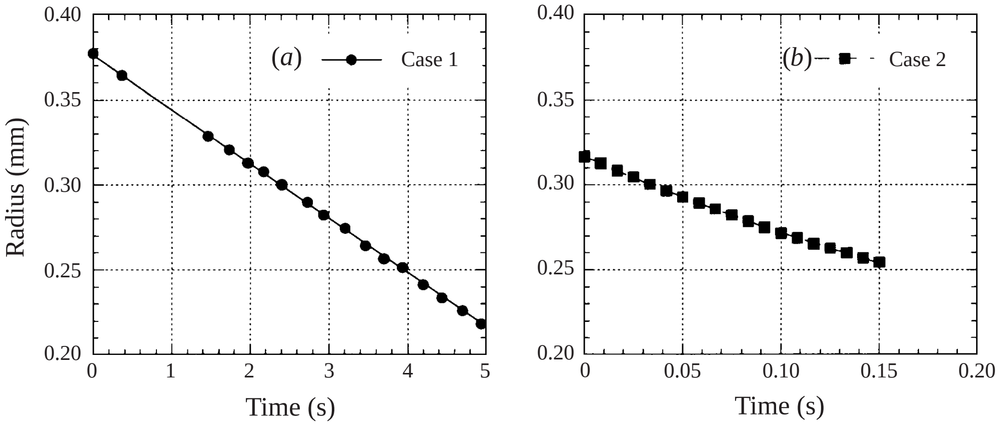

FIGURE 4. Time history of the bubble radius R.

shown by the line in figure 4 (*b*). The correlation is better than 0.999 for each curve and the maximum deviation of the fitted value from the experimental value is less than 2 %. We estimated the rate of radius change from the time differential of these fitted functions.

When we estimate p_g, we must consider the static liquid pressure and the surface tension. In particular, large errors result if we neglect the static liquid pressure when the concentration at infinity is high. For example, the pressure at the bottom of the column is atmospheric pressure (101.0 kPa) plus 5 kPa when the liquid height is 500 mm and the density is 997 kg m^{-3}. Therefore, the difference between the pressure of carbon dioxide inside the bubble, p_g, and the pressure of dissolved carbon dioxide in the water, $p_\infty = 70$ kPa, is about 35 kPa. On the other hand, at the top of the column $p_g - p_\infty = 30$ kPa. Therefore, we incur an error of 15 % if we neglect the static liquid pressure at the bottom of the column. We estimated the position of the bubble by time integration of U and then estimated the static liquid pressure.

The surface tension generally decreases by around 50 % from the value of the pure water due to contaminants. However, the resulting pressure change in the bubble is at most 0.5 kPa for our smallest bubble size of 0.15 mm. Therefore, we neglected changes of the surface tension and treated it as uncertainty.

Finally, we estimated *Sh* from (3.6). The maximum uncertainty in *Sh* is estimated to be 8 % by considering error analysis that includes R, the rate of radius change, the solubility, the diffusivity, and other experimental factors.

4. Numerical analysis of the dissolution process of the stagnant cap model

When we assume that the effect of the flow inside a bubble on the dissolution process is small and that mass transfer at the gas–liquid interface is sufficiently smooth, we only need to calculate the velocity and concentration field around the bubble to estimate *Sh*. According to the experimental results, we can assume that the bubble is spherical and that the flow around it is axially symmetric when we calculate the dissolution under our experimental conditions. We can also neglect the unsteady term in the Navier–Stokes equation and the convection–diffusion equation because we can assume that the velocity and concentration fields reach steady states. Therefore, we only solved the two-dimensional, axisymmetric, steady Navier–Stokes equation for the motion of the bubble, and we solved a steady convection–diffusion equation in spherical coordinates to calculate the velocity and concentration fields of the stagnant cap model.

4.1. *Governing equations*

Setting $u^* = u/U, r^* = r/R, c^* = (c - c_\infty)/(c_s - c_\infty), p^* = p/(\rho_l U^2)$, the equation of continuity, the Navier–Stokes equations, and the convection–diffusion equation can be written as follows:

$$\left.\begin{aligned} &\nabla \cdot \boldsymbol{u}^* = 0, \\ &\boldsymbol{u}^* \cdot \nabla \boldsymbol{u}^* = -\nabla p^* + \frac{2}{Re}\nabla^2 \boldsymbol{u}^*, \\ &\boldsymbol{u}^* \cdot \nabla c^* = \frac{2}{Pe}\nabla^2 c^*. \end{aligned}\right\} \tag{4.1}$$

We used the following boundary conditions in the stagnant cap model of Sadhal & Johnson (1983) and Fdhila & Duineveld (1996) (see figure 1):

$$\left.\begin{aligned} &u_r^* = 0 && (r^* = 1), \\ &\tau_{r\theta}^* = \frac{\partial}{\partial r^*}\left(\frac{u_\theta^*}{r^*}\right) = 0 && \left(r^* = 1, 0 \leqslant \theta \leqslant \theta_{cap}\right), \\ &u_\theta^* = 0 && \left(r^* = 1, \theta_{cap} < \theta \leqslant 180\right), \\ &u_r^* = -\cos\theta, \quad u_\theta^* = -\sin\theta && (r^* \to \infty), \\ &c^* = 1 && (r^* = 1), \\ &c^* = 0 && (r^* \to \infty), \end{aligned}\right\} \tag{4.2}$$

The drag coefficient and Sh can be expressed as follows (Clift *et al.* 1978):

$$\left.\begin{aligned} C_D \;=\;& 4\int_0^{\theta_{cap}} \left(p^* - \frac{4}{Re}\frac{\partial u_r^*}{\partial r^*}\right)_s \cos\theta \sin\theta \,\mathrm{d}\theta \\ &+ 4\left\{\int_{\theta_{cap}}^{\pi} p_s^* \cos\theta\sin\theta\,\mathrm{d}\theta + \int_{\theta_{cap}}^{\pi} \frac{2}{Re}\left(\frac{\partial u_\theta^*}{\partial r^*}\right)_s \sin^2\theta\,\mathrm{d}\theta\right\}, \\ Sh \;=\;& -\int_0^{\pi}\left(\frac{\partial c^*}{\partial r^*}\right)_s \sin\theta\,\mathrm{d}\theta. \end{aligned}\right\} \tag{4.3}$$

In this calculation, the concentration boundary layer is much thinner than the momentum boundary layer because $Sc = 500$. For increasing Péclet number Pe, to capture the thinner boundary layer the fineness of the grid and the number of grid points around the bubble were increased. We transformed the Navier–Stokes equation and the convection–diffusion equation as follows:

$$r^* = \frac{1}{(1-y)^a}, \tag{4.4}$$

where here

$$a = \left(\frac{100}{Pe}\right)^{1/3} \; (Pe \geqslant 100), \quad a = 1 \; (Pe < 100, Re < 100).$$

The above equations were differentiated by the K–K scheme (Kawamura & Kuwahara 1983), which is a third-order upwind scheme, and solved by the SOR method. We divided the calculation domain into 100 grid points in the radial direction and 60 grid points in the tangential direction.

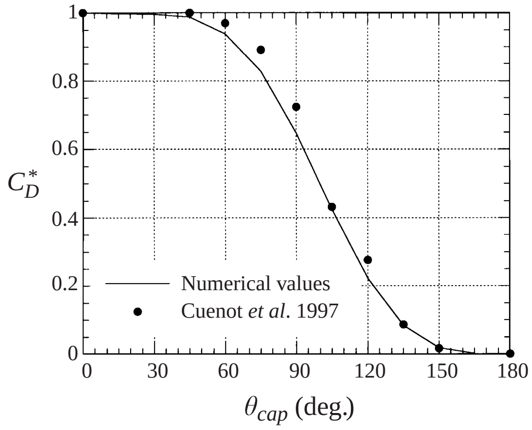

FIGURE 5. Drag coefficient C_D^* for $Re = 100$ as a function of stagnant cap angle θ_{cap}.

4.2. *Uncertainties of numerical results*

We estimated the uncertainties of numerical values of the drag coefficients by comparing our values with those by Cuenot *et al.* (1997). Figure 5 shows the drag coefficients at $Re = 100$ as a function of stagnant cap angle (θ_{cap}). We normalized the drag coefficients as follows:

$$C_D^* = \frac{C_D - C_{D,FS}}{C_{D,SP} - C_{D,FS}}, \tag{4.5}$$

where the subscript *SP* denotes solid particle and *FS* denotes fluid sphere. Figure 5 shows that our numerical results have sufficient accuracy because the maximum deviation between our results and the results of Cuenot *et al.* (1997) is 7 %. This confirms that the effects of the unsteady term on the drag coefficients are small because the results of Cuenot *et al.* (1997) include the unsteady term. We have also confirmed that our model has acceptable accuracy for estimating the dissolution rate at $Pe = 10^7$ (Takemura & Yabe 1998).

5. Results of drag coefficient and Sherwood number affected by contamination

Figure 6 shows the value of C_D normalized by the Hadamard–Rybczynski solution ($16/Re$) as a function of Re. For comparison, we also show the drag coefficient of air bubbles in methanol, the drag equation for a fluid sphere proposed by Mei *et al.* (1994), and the drag equation for a solid particle proposed by Clift *et al.* (1978). The available expressions for calculating C_D are as follows:

$$C_{D,FS} = \frac{16}{Re}\left[1 + \left\{\frac{8}{Re} + \frac{1}{2}\left(1 + \frac{3.315}{Re^{0.5}}\right)\right\}^{-1}\right], \tag{5.1}$$

$$C_{D,SP} = \frac{24}{Re}\left(1 + 0.1935Re^{0.6305}\right). \tag{5.2}$$

Figure 6 shows that although the drag coefficient of air bubbles in methanol coincides with that of a fluid sphere, the drag coefficient of carbon dioxide bubbles in water is much greater than that of fluid spheres, and coincides with that of solid

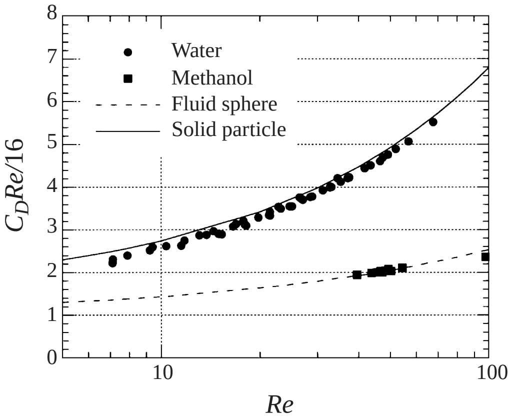

FIGURE 6. Drag coefficient $C_DRe/16$ as a function of Reynolds number *Re*.

particles. Clift *et al.* (1978) reported that the drag coefficient of air bubbles in water is the same as for solid particles, due to contamination at the gas–liquid interface. Our results confirm this behaviour. Of course, even for water, the drag coefficients are the same as for fluid spheres when one uses hyper clean water (Duineveld 1995). In our experiments, we use relatively clean water produced by ion exchangers and filters, but it was not pure, and the drag coefficients are affected by even slight contamination. The resulting bubble drag coefficients were similar to those of solid particles.

The drag coefficient of bubbles in water is the same as for solid particles. If the velocity and the concentration fields around the bubbles in the water are the same as for particles, *Sh* for the bubble is the same as for the solid particle based on the velocity and the concentration fields around the solid particle when we assume that the effect of flow inside the bubble on the dissolution process is small and that mass transfer at the gas–liquid interface is sufficiently smooth. Figure 7 shows the experimental and the numerical results as circles and solid lines, respectively. The numerical results agree with the experimental result within 3 %. The numerical results simulate well the dissolution process of a spherical gas bubble and show that the concentration fields around the bubble are the same as the concentration fields around the solid particle, and that the interface is immobile. Lochiel & Calderbank (1964) give the following analytical solution for *Sh* of a solid particle using the distribution of the gradient of velocity at the interface:

$$Sh = 0.641 \left[\int_0^{\pi} \left\{ \left(\frac{\partial u_\theta^*}{\partial r^*} \right)_{r^*=1} \sin^3\theta \right\}^{1/2} \mathrm{d}\theta \right]^{2/3} Pe^{1/3}. \tag{5.3}$$

Sh for high *Sc* is obtained by substituting the velocity gradient distribution at the surface calculated numerically into (5.3), which shows that one cannot calculate *Sh* in the regime where separations occur. Clift *et al.* (1978) reported that separation occurs for flow around solid particles when $Re > 20$. Therefore, (5.3) can be applied safely for $Re < 20$. Figure 7 shows the value of *Sh* calculated from our experimental data and obtained by substituting the velocity gradient distribution calculated from the velocity distribution around a solid particle when $Sc = 500$: the values of *Sh* determined with (5.3) agree with the measured values.

When the interface is immobile, the equation for predicting *Sh* is given by correlating

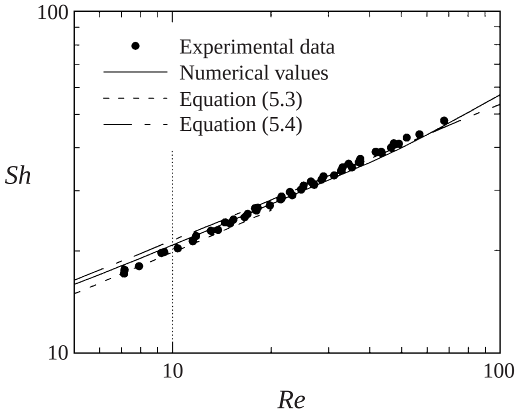

FIGURE 7. Sherwood number Sh as a function of Reynolds number Re.

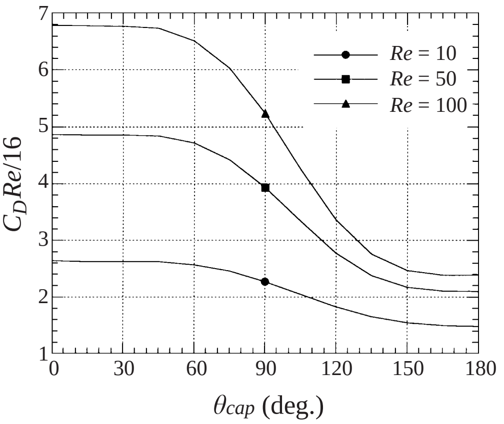

FIGURE 8. Numerical drag coefficient C_D^* as a function of stagnant cap angle θ_{cap}.

numerical results and is expressed as follows (Clift *et al.* 1978):

$$Sh = 1 + (Pe + 1)^{1/3} Re^{0.077}. \tag{5.4}$$

Figure 7 also shows the values of Sh calculated from (5.4), which agree with the experimental results for $Re > 5$. Moreover, the contaminants attached to the interface do not restrict the dissolution of carbon dioxide when the bubble rises in slightly contaminated water, such as we used.

6. Effects of stagnant cap angle on drag coefficient and Sherwood number

Figure 8 shows the drag coefficient as a function of stagnant cap angle (θ_{cap}): the drag coefficient increases as θ_{cap} decreases from 180 to 0, thus the stagnant cap develops from the rear of the bubble. Because the interface becomes immobile from the rear, the drag increases by a factor of about 2.5 and 4.5 for $Re = 50$ and 100, respectively, where separations occur at the rear of the bubble (Clift *et al.* 1978). In each case, the drag coefficient increases from $\theta_{cap} = 150$ and the maximum gradients occur at about $\theta_{cap} = 105$. The gradients then become shallow, and at $\theta_{cap} = 60$ the drag coefficients approach the values for the solid particles. These results agree with those by Cuenot *et al.* (1997).

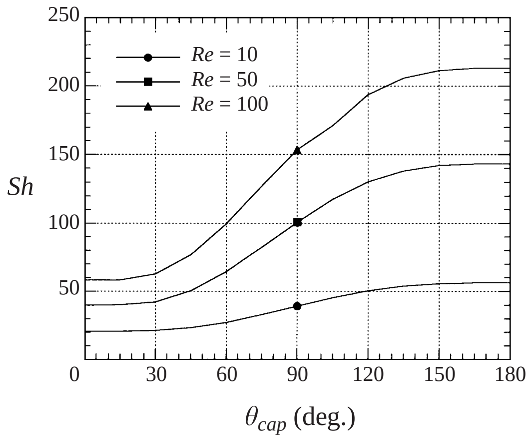

FIGURE 9. Sherwood number Sh as a function of stagnant cap angle θ_{cap}.

Figure 9 shows Sh as a function of θ_{cap}: Sh decreases as θ_{cap} decreases from 180 to 0. This decrease occurs because the interface becomes immobile from the rear and the convection near the surface becomes weak. In each case, Sh decreases from $\theta_{cap} = 150$ and the maximum gradients occur near $\theta_{cap} = 90$. The gradients then become shallow, and at $\theta_{cap} = 30$, Sh approaches the value for solid particles.

Both figures 8 and 9 show that the drag coefficient and Sh vary in the transition regime from a fluid sphere to a solid particle. Therefore, we can compare the numerical and experimental results for the drag coefficient and Sh even if we allow for the uncertainties of the experimental results.

7. Comparison between numerical and experimental results

Figure 10 shows Sh as a function of drag coefficient. The dotted lines show the numerical results for constant Re and θ_{cap}. The symbols and solid lines show the experimental results. We selected the experimental data where Re corresponds as closely as possible with the numerical values. Symbols of the same type correspond to the same experiment, and Re and the frame number F from the initial frame are shown for each data point. The frame number multiplied by 1/120 s gives the passage time from the initial frame.

Figure 10 shows that the experimental and numerical values for Sh are in good agreement for similar Re and drag coefficients, and that θ_{cap} decreases with time. These results quantitatively demonstrate that the stagnant cap model can express the transition process in a bubble's behaviour from a fluid sphere to a solid particle.

Figure 11 shows Sh as a function of drag coefficient, normalized as follows:

$$C_D^* = \frac{C_D - C_{D,FS}}{C_{D,SP} - C_{D,FS}}, \quad Sh^* = \frac{Sh - Sh_{FS}}{Sh_{SP} - Sh_{FS}}. \tag{7.1}$$

We calculated $C_{D,SP}$ and $C_{D,FS}$ using (5.1) and (5.2), Sh_{SP} using (5.4), and Sh_{FS} using the equation (Takemura & Yabe 1998)

$$Sh = \left(\frac{4}{\pi}\right)^{1/2} \left\{ 1 - \frac{2}{3} \frac{1}{\left(1 + 0.09Re^{2/3}\right)^{3/4}} \right\} \left(2.5 + Pe^{1/2}\right). \tag{7.2}$$

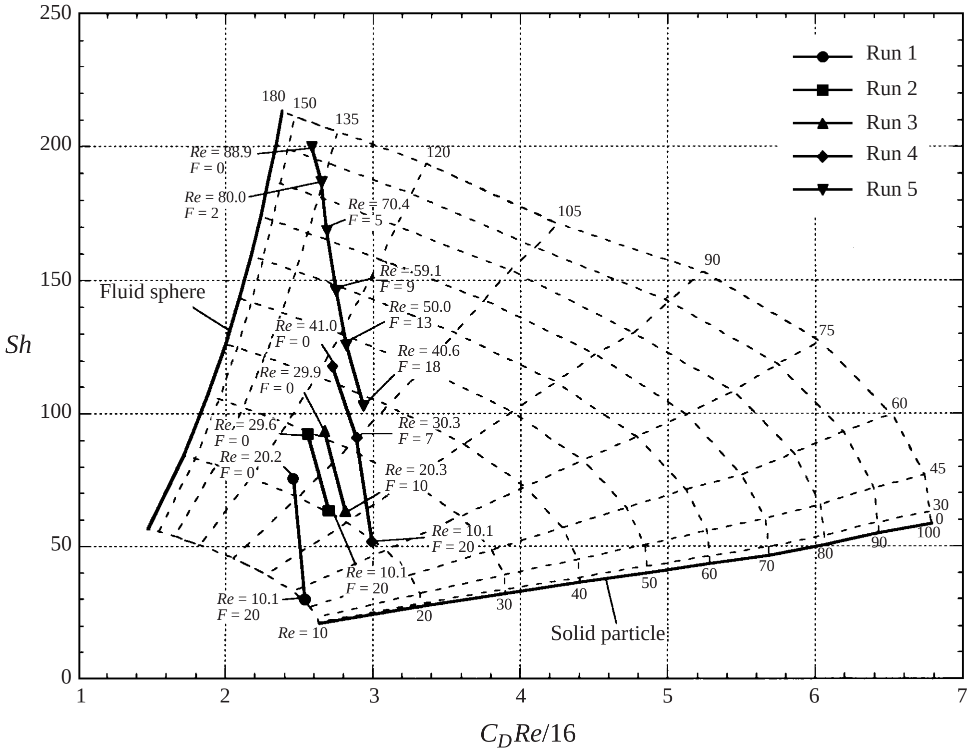

FIGURE 10. Sherwood number Sh as a function of drag coefficient $C_DRe/16$.

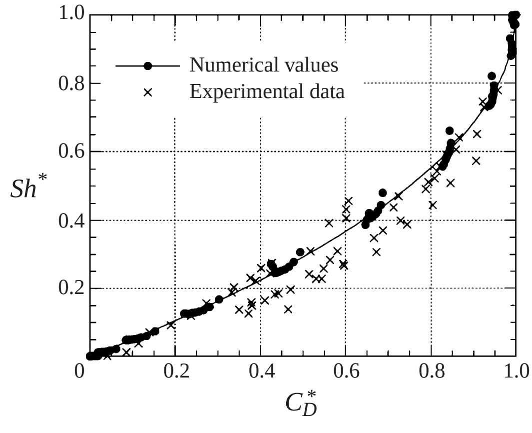

FIGURE 11. Sherwood number Sh^* as a function of drag coefficient C_D^*.

The circles in figure 11 show the numerical results and the line shows the curve fitted to these numerical results. The normalized Sh can be estimated by a simple function of C_D^*:

$$1 - Sh^* = \left(1 - C_D^*\right)^{1/2}. \tag{7.3}$$

The maximum deviation between values calculated using (7.3) and the numerical results is 5 %, except near $C_D^* = 1$. The crosses show the experimental results. Figure 11 quantitatively validates the stagnant cap model.

8. Summary

We developed an experimental apparatus in which a charged-coupled device (CCD) camera with a microscope follows a rising bubble and precisely measures the changes in R and U. We used this device to observe a spherical carbon dioxide gas bubble dissolving in slightly contaminated water. We estimated Sh as a function of Sc and Re based on the changes in R and U. We also numerically estimated the drag coefficients and Sherwood number of the stagnant cap model by directly solving the Navier–Stokes equation for flow around the bubble and the convection–diffusion equation for gas transport across the bubble–liquid interface. The results reveal that the drag coefficients of the bubble are similar to those of solid particles for even a small amount of contamination. The concentration fields around the bubble affected by contamination are the same as the concentration fields around solid particles and the interface is immobile. We also demonstrated that the experimental and numerical results agree well in the transition regime where the bubble changes behaviour from a fluid sphere to a solid particle and the stagnant cap model can explain quantitatively the mechanism of this transition process.

REFERENCES

Benedict, R. P., Abernethy, R. B., Osolsobe, G. *et al.* 1985 Measurement uncertainty. *ANSI/ASME PTC* 19-1.

Brankovic, A., Currie, I. G. & Martin, W. W. 1984 Laser-Doppler measurements of bubble dynamics. *Phys. Fluids* **27**, 348–355.

Calderbank, P. H., Johnson, S. L. & Loudon, J. 1970 Mechanics and mass transfer of single bubbles in free rise through some Newtonian and non-Newtonian liquid. *Chem. Engng Sci.* **25**, 235–256.

Christov, C. I. & Volkov, P. K. 1985 Numerical investigation of the steady viscous flow past a stationary deformable bubble. *J. Fluid Mech.* **158**, 341–364.

Clift, R., Grace, J. R. & Weber, M. E. 1978 *Bubbles, Drops and Particles.* Academic.

Cuenot, B., Magnaudet, J. & Spennato, B. 1997 The effects of slightly soluble surfactants on the flow around a spherical bubble. *J. Fluid Mech.* **339**, 25–53.

Detsch, R. & Harris, I. 1989 Dissolution and rise velocity of small air bubbles in water and salt water. *Oceans '89, Part 1. IEEE*, pp. 286–291.

Duineveld, P. C. 1995 The rise velocity and shape of bubbles in pure water at high Reynolds number. *J. Fluid Mech.* **292**, 325–332.

Fdhila, R. B. & Duineveld, P. C. 1996 The effect of surfactant on the rise of a spherical bubble at high Reynolds and Peclet number. *Phys. Fluids* **8**, 310–321.

Himmelblau, D. M. 1956 Diffusion of dissolved gases in liquids. *Chem. Rev.* **64**, 527–550.

Kawamura, T. & Kuwahara, K. 1984 Computation of high Reynolds number flow around a circular cylinder with surface roughness. *AIAA Paper* 84-0340.

Leonard, J. H. & Houghton, G. 1963 Mass transfer and velocity of rise phenomena for single bubbles. *Chem. Engng Sci.* **18**, 133–142.

Lochiel, A. C. & Calderbank, P. H. 1964 Mass transfer in the continuous phase around axisymmetric bodies of revolution. *Chem. Engng Sci.* **19**, 471–484.

Mei, R., Klausner, J. F. & Lawrence, C. J. 1994 A note on the history force on a spherical bubble at finite Reynolds number. *Phys. Fluids* **6**, 418–420.

Ryskin, G. & Leal, L. G. 1984 Numerical solution of free-boundary problems in fluid mechanics. *J. Fluid Mech.* **148**, 1–17.

Sadhal, S. S. & Johnson, R. E. 1983 Stokes flow past bubbles and drops partially coated with thin films. *J. Fluid Mech.* **126**, 237–250.

SENGERS, J. V. & WATSON, J. T. R. 1986 Improved international formulations for the viscosity and thermal conductivity of water substance. *J. Phys. Chem. Ref. Data* **15**, 1291–1314.

TAKAGI, S. & MATSUMOTO, Y. 1996 Force acting on a rising bubble in a quiescent liquid. *Proc. ASME Summer Meeting on Numerical Methods for Multiphase Flow* (ed. I. G. Crow *et al.*) vol. 1, pp. 575–580.

TAKEMURA, F. & YABE, A. 1998 Gas dissolution process of spherical rising gas bubbles. *Chem. Engng Sci.* **53**, 2691–2699.

UCHIDA, H. *et al.* 1982 *JSME Data Book: Thermophysical Properties of Fluids.* Japanese Society of Mechanical Engineers.

WILHELM, E., BATTINO, R. & WILCOCK, R. J. 1977 Low-pressure solubility of gases in liquid water. *Chem. Rev.* **77**, 219–262.